Diagnosis of the Three-Dimensional Circulation Associated with Mesoscale Motion in the California Current

R. KIPP SHEARMAN, JOHN A. BARTH, AND P. MICHAEL KOSRO

College of Oceanic and Atmospheric Sciences, Oregon State University, Corvallis, Oregon

(Manuscript received 3 October 1997, in final form 20 April 1998)

ABSTRACT

A high-resolution upper-ocean survey of a cyclonic jet meander and an adjacent cyclonic eddy in the California Current region near 38°N, 126°W was conducted as part of the summer of 1993 Eastern Boundary Currents program. Temperature and salinity were measured from a SeaSoar vehicle, and velocity was measured by shipboard acoustic Doppler current profiler (ADCP). SeaSoar data show a density front at a depth of 70–100 m with strong cyclonic curvature. The geostrophic velocity fields, referenced to the ADCP data at 200 m, show a strong surface-intensified jet (maximum speed of 0.9 m s^{-1}) that follows the density front along a cyclonic meander. Relative vorticities within the jet are large, ranging from $-0.8f$ to $+1.2f$, where f is the local Coriolis parameter. The SeaSoar density and ADCP velocity data are used to diagnose the vertical velocity via the Q-vector form of the quasigeostrophic omega equation. The diagnosed vertical velocity field shows a maximum speed of 40–45 m d^{-1}. The lateral distribution of vertical velocity is characterized by two length scales: a large (~75 km) pattern where there is downwelling upstream and upwelling downstream of the cyclonic bend, and smaller patches arrayed along the jet core with diameters of 20–30 km. Geostrophic streamline analysis of vertical velocity indicates that water parcels make net vertical excursions of 20–30 m over 2–3 days, resulting in net vertical velocities of 7–15 m d^{-1}. Water parcels moving along geostrophic streamlines experience maximum vertical velocities in the regions of maximum alongstream change in relative vorticity, an indication of potential vorticity conservation.

1. Introduction

Research over the last twenty years has uncovered the importance of mesoscale motion in eastern boundary currents, particularly in the California Current System (CCS) off the west coast of the United States. Experiments such as the California Cooperative Oceanic Fisheries Investigation (CalCOFI) (Wyllie 1966), the Coastal Ocean Dynamics Experiment (CODE) (Huyer and Kosro 1987), and the Coastal Transition Zone experiment (CTZ) (Brink and Cowles 1991; Strub et al. 1991) have helped to redefine our view of the CCS from a diffuse, broad, weak flow to a seasonally energetic, complex flow rich with mesoscale variability. While the existence of mesoscale motion was indicated by CalCOFI observations, the coarseness and nonsynopticity of the CalCOFI surveys did not actually resolve distinct mesoscale features. The existence and importance of mesoscale motion in the CCS were clearly demonstrated during CODE and later in CTZ. However, measurements were still too widely spaced to fully resolve the density and velocity structures associated with mesoscale features such as jet meanders and eddies. Likewise, the dynamics associated with these mesoscale features could only be inferred from the coarse observations, and estimating the full three-dimensional circulation associated with eddies and jet meanders in the CCS was beyond the scope of past experiments.

Estimating the full three-dimensional circulation in the ocean is complicated by the difficulty in measuring the vertical velocity w. Horizontal velocities in the CCS are vigorous (0.5–0.8 m s^{-1}) and highly geostrophic (Kosro and Huyer 1986). Thus, horizontal velocities are relatively simple to measure, either from density profiles and the thermal wind relation or through the use of a shipboard acoustic Doppler current profiler (ADCP). Vertical velocities in the ocean are nearly impossible to directly measure over a wide area (as would be needed for the study of mesoscale features). Measurements of the divergent component of the horizontal flow are unresolved by shipboard ADCP. Ageostrophic currents in the CCS are typically 0.02–0.04 m s^{-1} (Kosro 1987; Chereskin 1995), while resolution of the shipboard ADCP varies from 0.03 to 0.05 m s^{-1}, depending on processing techniques (Kosro 1987; Kosro et al. 1991).

An alternate method is needed for estimating vertical velocity that can be made from fields that can be mea-

Corresponding author address: Dr. R. Kipp Shearman, Oregon State University, College of Oceanic and Atmospheric Sciences, Oceanography Admin. Bldg. 104, Corvallis, OR 97331.
E-mail: kshearma@oce.orst.edu

sured accurately. The quasigeostrophic (QG) omega equation in its Q-vector formulation (Hoskins et al. 1978) requires only a single synoptic realization of the three-dimensional density field to diagnose the associated vertical velocities. The QG omega equation was originally developed in the atmospheric context but has recently found applications in oceanography (Pollard and Regier 1992; Rudnick 1996; Allen and Smeed 1996). Pollard and Regier (1992) used a two-dimensional version of the omega equation that ignored along-front variations to diagnose the ageostrophic circulation in a vertical plane. Most recently, Rudnick (1996) and Allen and Smeed (1996) have used the full three-dimensional omega equation to diagnose the vertical velocities at the Azores and Iceland–Færoes Fronts, respectively. Also, Chumbinho (1994) compares a diagnosis of w via the Q-vector equation to a diagnosis of w using a primitive equation model and a digital filtering technique.

The purpose of this paper is to establish estimates of the vertical velocities associated with mesoscale features, such as jets and eddies, in the CCS. To determine these vertical velocities, the Q-vector analysis will be applied to a high-resolution survey of the density and horizontal velocity fields within the CCS, conducted as part of the summer 1993 Eastern Boundary Currents (EBC) project. From these estimates, we gain a clearer picture of the three-dimensional circulation within these mesoscale features and may investigate their underlying dynamics. Understanding the role of vertical velocity in the dynamics of mesoscale features is necessary to elucidate the importance of eddies and concentrated jets in the changing view of the CCS. In addition, estimates of vertical velocities associated with mesoscale features have important consequences (in terms of the vertical transport) for the biology and chemistry in this region.

The remainder of this paper is organized as follows: section 2 describes the datasets and sampling methods; section 3 provides a detailed description of the analysis methods and their results, including the interpolation of the density and ADCP data onto regular grids; section 4 describes the calculated geostrophic velocity and relative vorticity fields; section 5 covers the diagnosis of vertical velocity; section 6 discusses the results and examines the full three-dimensional pathways of water parcels passing through the region; and section 7 summarizes the preceding material.

2. Dataset

The 1993 EBC project consisted of two large-scale surveys and four small-scale surveys of physical and biological fields within the California Current offshore of northern California. The first large-scale survey was conducted during 7–28 June and the second during 8 August–1 September. These surveys were composed of zonal sections 350–450 km long, running from the 1000-m isobath to the deep ocean, separated by 28 km in the north–south direction, and covering a region from 36°N (large-scale survey 1) or 37°N (large-scale survey 2) to 39°N. A detailed description of the hydrographic fields observed during the large-scale surveys can be found in Huyer et al. (1998).

In addition, four small-scale surveys of individual features were conducted as part of the EBC project. Hydrographic data from the large-scale surveys and satellite sea surface temperature (SST) images were used to locate features of interest. The first small-scale survey (SS1) was carried out over 29 June–2 July and sampled an offshore cyclone and oceanic jet meander. These features can be seen in relation to the larger CCS within the boxed region in Fig. 1. The meandering jet—associated with the core of the CCS—sampled during SS1 and apparent in the SST image (Fig. 1) carries a large portion of the equatorward transport identified with the California Current.

A second small-scale ''survey,'' conducted during 6–7 July, sampled the same cyclone and jet meander but only along one across-front transect. The third small-scale survey was carried out over 1–5 September and sampled a counterrotating eddy pair, an offshore cyclone (the same cyclone as sampled in SS1) adjacent to an inshore anticyclone. Finally, the fourth small-scale survey, carried out over 6–16 September, sampled a deep, inshore anticyclone. This paper discusses the results of the analysis applied to measurements made during SS1, leaving the analysis of the additional small-scale surveys to a future study.

The primary instruments used to sample physical fields during the EBC project were the SeaSoar, a towed undulating measurement platform (Pollard 1986), and shipboard ADCP. The SeaSoar was outfitted with a Seabird conductivity–temperature–depth (CTD) sensor, as well as other instruments to sample biological fields (Cowles et al. 1994; Huntley et al. 1995). The SeaSoar vehicle completed an undulation cycle approximately once every 9 minutes, and was towed at a nominal speed of 8 kt ($\sim$4 m s^{-1}). This translates into an alongtrack resolution of 2.2 km at the surface and bottom of the sawtooth-shaped SeaSoar trace and approximately half of that (1.1 km) at middepth. The SeaSoar undulated consistently between the surface and deeper than 300 m. The ship's flow-through CTD located at a depth of 5 m was used to supplement the SeaSoar data near the surface. The raw 24-Hz SeaSoar CTD data were time averaged into 4-Hz data, which were then averaged into 2-dbar bins. A summary of SeaSoar CTD data processing can be found in Huyer et al. (1998), and a complete description is contained in the data report by Kosro et al. (1995). Absolute currents were measured continuously during each survey, using an RD Instruments 150-kHz ADCP. Average velocity profiles, using an 8-m bin size, were obtained every 2.5 minutes, which at 8 kt is equivalent to an alongtrack resolution of less than 1 km. The average velocity profiles were subsequently low-pass filtered using a filter with half-power at 30

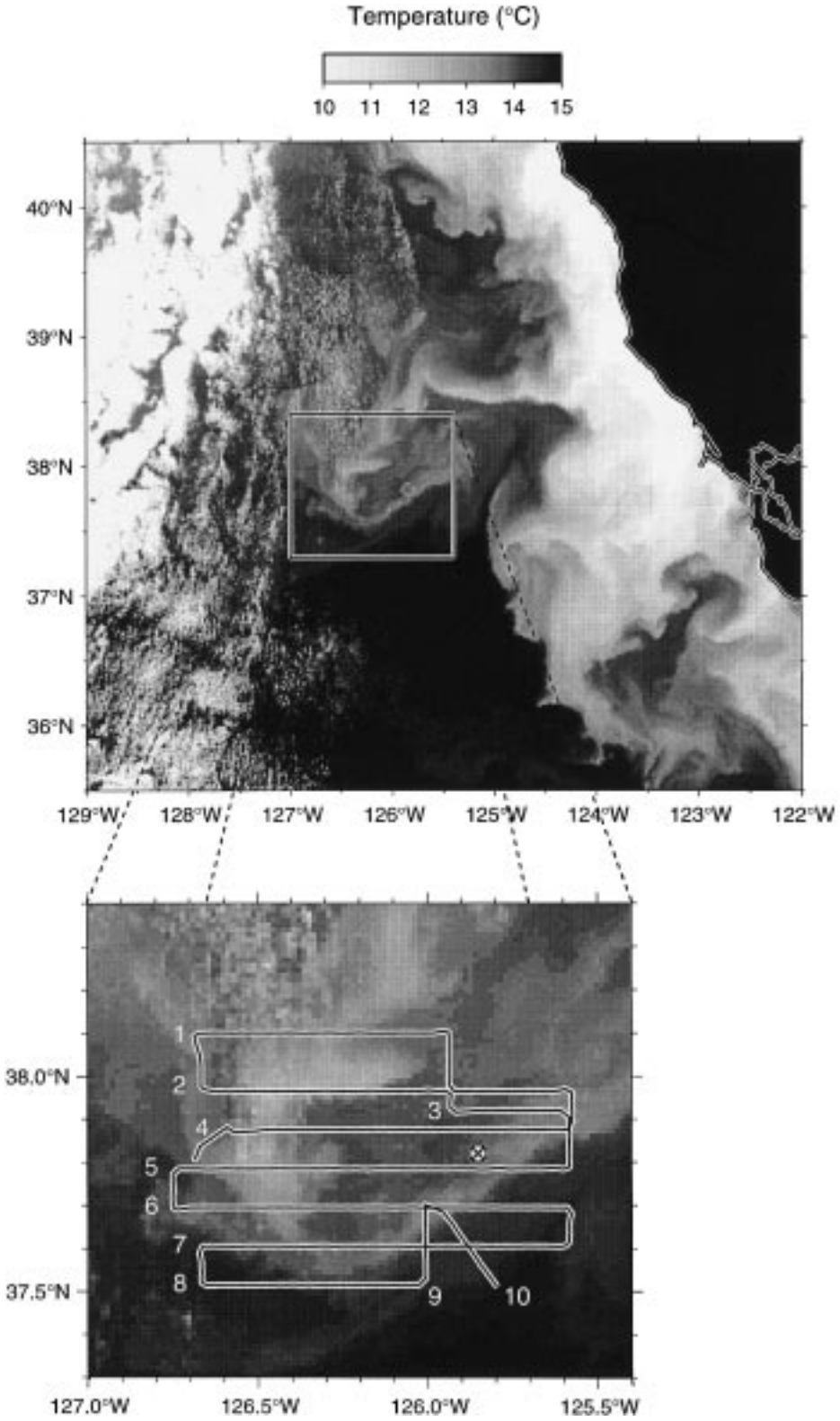

FIG. 1. (top) Satellite SST image (2300 UTC 29 June 1993) with SS1 region boxed. A cold filament originating in the vicinity of 38.5°N, 124°W extends offshore and into the SS1 survey region, where it makes a strong cyclonic turn. (bottom) The boxed region is expanded and the ship track for SS1 is overlaid. Lines are numbered 1–10, and the location of the mooring is indicated by a circled cross ⊗.

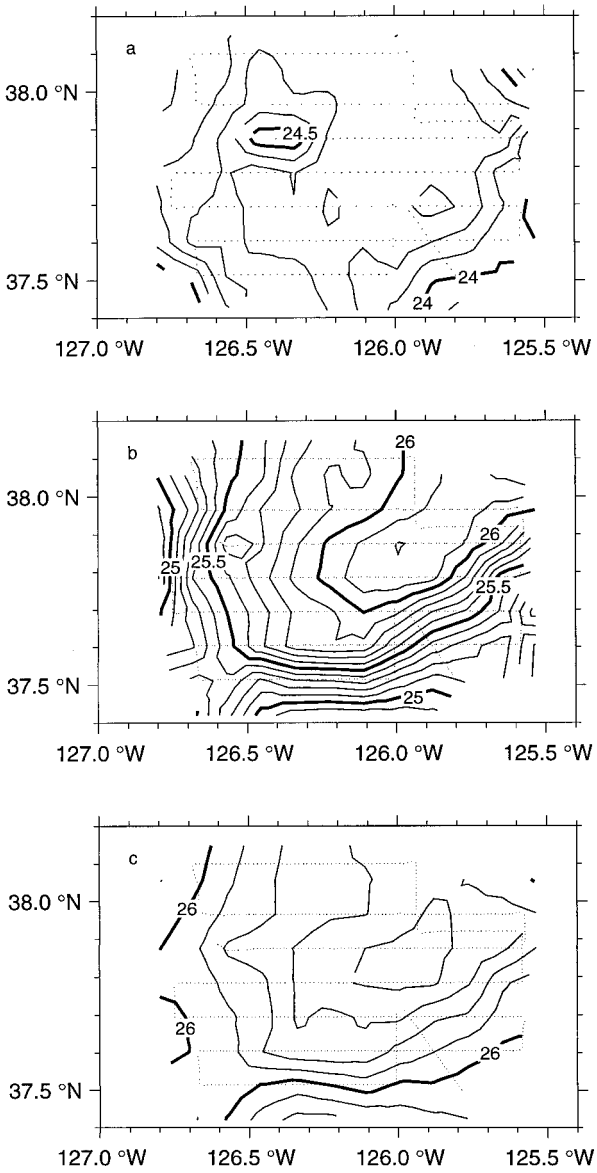

FIG. 2. Maps of raw SeaSoar-derived σ_t (kg m^{-3}) at depths of (a) 15 m, (b) 101 m, and (c) 151 m. The location of SeaSoar measurements are shown as small dots. There are an average of 644 data points at each vertical level.

min. The shallowest bin to consistently return velocity data was about 25 m and the deepest was about 350 m.

In addition to the shipbased observations, a single mooring—part of the California Current Moored Array (Chereskin et al. 1994)—was located within the SS1 survey region at 37.82°N, 125.85°W in 4320 m of water. The mooring was equipped with three Aanderaa Current Meters (AACMs), which recorded current speed and direction, every 3 hours over a 2-yr period beginning in August 1992. At each AACM location there were also a thermistor and pressure sensor. The AACMs were deployed at depths of 150, 300, and 600 m. However, records from the pressure sensors collocated with the AACMs have means of 142, 295, and 602 dbar, respectively. The location of the mooring relative to the cyclone and jet meander can be seen in Fig. 1.

Small-scale survey 1, on which the rest of this paper will focus, consisted of eight zonal sections approximately 100 km long, separated by 10 km in the north–south direction (see the enlarged region in Fig. 1). In addition, one 20 km meridional section and a 30 km diagonal section—running roughly perpendicular to the density front at this location—were occupied. The survey region covered a rectangular area from 37.5° to 38.1°N, 125.6° to 126.8°W and from (approximately 100 km by 70 km). The entire survey took 60 hours to complete.

The horizontal distribution of density as measured by SeaSoar (see Fig. 2) shows a front that has been deformed into a strong cyclonic meander. The curved front is strongest between the depths of 70 and 110 m (Fig. 2b) but is evident down to at least 310 m (the deepest level of consistent horizontal coverage). The curved front weakens as it deepens (cf. Figs. 2b and 2c). Between 40 and 60 m there are strong gradients in the density field; however, they do not exhibit the coherent cyclonic meander structure present below. The horizontal distribution of density above 40 m is much more homogeneous, although in the southeast corner of the survey region the density front appears weakly at the surface (Fig. 2a). Also, there is a highly localized pocket of dense water ($\sigma_t \geq 24.3$ kg m^{-3}) approximately 30 km in diameter centered on the west end of line 4 (see Fig. 1 for definition of line numbers).

The vertical distribution of density as measured by SeaSoar shows domed isopycnals near the center of the region corresponding to the location of the cyclonic eddy (Fig. 3). The thickness of the homogeneous surface mixed layer ranges from 20 to 40 m, and tends to be shallower over the jet and deeper over the cyclone (see Fig. 3b). Buoyancy frequency N in cph, calculated from the slope of a line fit to the raw SeaSoar σ_t data over a 12-dbar bin, is also shown in Fig. 3. Stratification is strongest (12 cph) at the base of the mixed layer over the cyclonic eddy at a depth of approximately 50 m. In lines 4 and 5 within the jet at a depth of approximately 100 m and a longitude of about 126.5°W, there is an anomalously thick layer of weakly stratified water between the isopycnals $\sigma_t = 25.4$ and 25.6 kg m^{-3}. The thickness anomaly extends approximately 15 km in the across-jet direction and 20 km in the alongjet direction. Stratification is weakest within the thickness anomaly at line 5 (Fig. 3b) and the thickness anomaly is no longer readily apparent by line 6 (Fig. 3c), 10 km downstream. Similar thickness anomaly features were reported at a density front in the Sargasso Sea by Pollard and Regier (1992).

3. Data reduction

Estimating vertical velocity via the Q-vector equation requires the calculation of high-order spatial derivatives

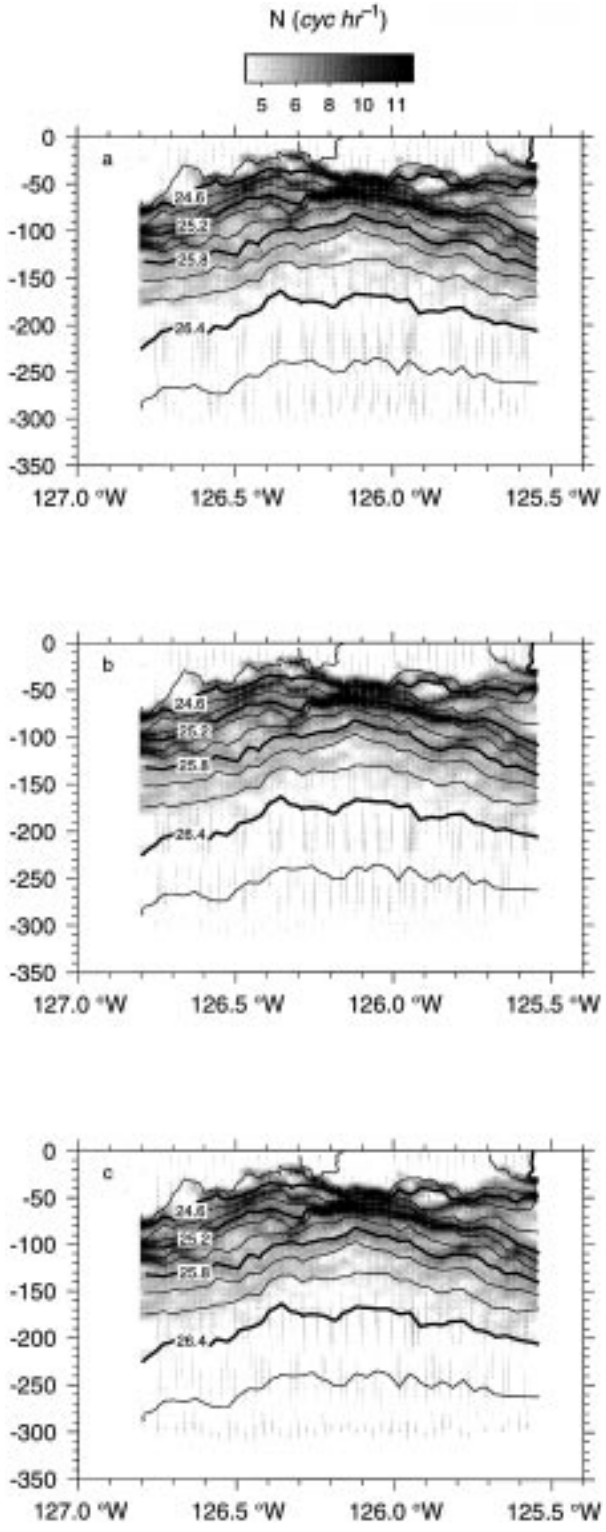

FIG. 3. Sections of raw SeaSoar-derived σ_t (kg m^{-3}) data (contours) and buoyancy frequency N (cyc h^{-1}) (shading) along (a) line 4, 37.87°N; (b) line 5, 37.78°N; and (c) line 6, 37.69°N. These lines pass roughly through the center of the cyclone/jet feature. The location of SeaSoar measurements are shown as small gray dots to highlight the alongtrack resolution. There are an average of 86 individual profiles (both uptrace and downtrace included) along each line.

of the density and geostrophic velocity fields. Therefore, we must grid and smooth the data to avoid amplifying small-scale noise. Interpolating the irregularly sampled SeaSoar and ADCP data onto regular grids simplifies the computation of spatial derivatives, and smoothing reduces the effect of small-scale spatial variations, such as internal waves and inertial oscillations, which are outside the scope of this analysis.

The data reduction procedures are similar for both SeaSoar density data and ADCP velocity data. First, we estimate a spatially variable mean. Then, we calculate a residual field by subtracting the mean field from the raw data and interpolate that residual onto a regular grid using standard objective analysis (OA) (Bretherton et al. 1976). Finally, we compute the total interpolated field by adding together the objectively analyzed residual and the mean field.

a. Density data

Individual profiles of the raw 2-dbar SeaSoar density data are averaged vertically into 10-m bins (σ_t^{bin}). The vertical bins are centered on 0, 10, 20, . . . , 310 m (for this analysis dbars and meters are treated as equivalent measures). The maximum pressure reached using SeaSoar never exceeds 500 dbar; hence the relative error between dbars and meters is always less than 1% (Fofonof and Millard 1983). Density data from the ship's flow-through CTD (intake at a depth of 5 m) are used to supplement the SeaSoar data at the surface where gaps in the coverage may occur. A visual synopsis of the data reduction procedures is found in Fig. 4. The σ_t^{bin} field at a depth of 100 m is shown in Fig. 4a. The bin-averaged field has slightly less small-scale variability than does the raw SeaSoar density data (cf. Fig. 2).

Standard OA is intended for use on fields with a stationary or spatially invariant mean (Bretherton et al. 1976). Our study area is characterized by a highly nonstationary mean (the curved density front). In order to find a stationary residual field (residual being defined as anything other than the mean), we must determine an appropriate spatially variable mean, and then remove that mean from the bin-averaged data. Otherwise, the signal from the small-scale residual field will be drowned out by the energetic large-scale mean.

The bin-averaged density data (Fig. 4a) indicate that the spatially variable mean is a curvilinear density front with strong cyclonic curvature. Previous studies (e.g., Walstad et al. 1991; Rudnick 1996) focused on linear density fronts without strong curvature. In each of these cases, the shape of the mean density (or dynamic height) field was given by a first-order polynomial fit to the raw data using a least squares method. Due to the strong curvature of the front in our case, a plane does not adequately represent the mean field. Instead, a second-order polynomial,

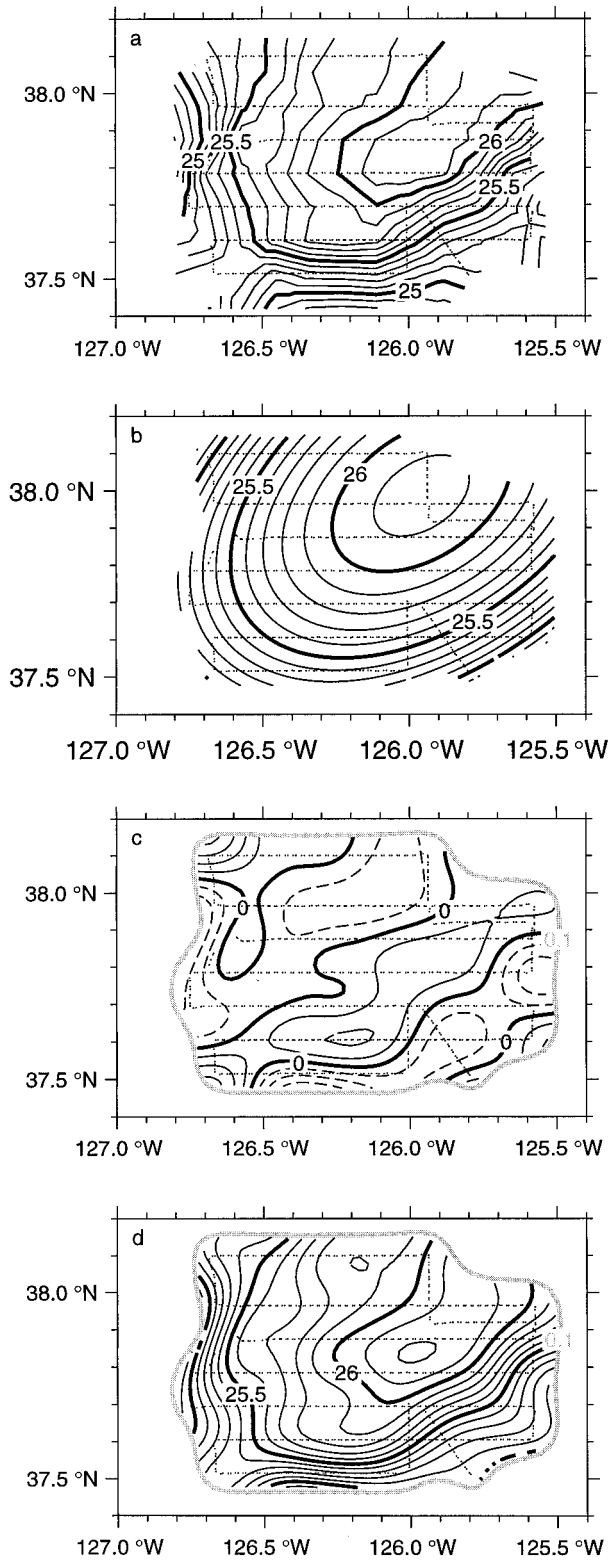

FIG. 4. Data reduction process for SeaSoar σ_t (kg m^{-3}) data at 100 m: (a) raw SeaSoar data vertically bin-averaged into 10-m bins; (b) polynomial representation of the mean field; (c) objectively analyzed residual field; and (d) total interpolated field. In the bottom two panels, fields are only shown where the OA error covariance is 0.1 or less.

TABLE 1. Results of the least squares tidal analysis.

	Amplitude (°C)	Phase (°)
Mooring 150 m	0.090	141.9
SeaSoar 150 m	0.073	88.7
Mooring 300 m	0.054	−151.6
SeaSoar 300 m	0.051	−129.2

$$\overline{\sigma_t} = Ax^2 + Bxy + Cy^2 + Dx + Ey + F, \quad (1)$$

is fit to the σ_t^{bin} data, and this function is used to describe the mean density field, signified by an overbar. In this analysis, the *x, y,* and *z* axes are oriented in the eastward, northward, and local vertical directions, respectively. The result of the least squares fit of a second-order polynomial to the σ_t^{bin} data at a depth of 100 m is shown in Fig. 4b. The fit is performed at each vertical level. Within the surface mixed layer (depth levels above 40 m), the mean field is flat, while in the deeper levels the mean field has a parabolic shape. We then calculate the residual field (σ_t^{res}) by subtracting the mean field from the bin-averaged data:

$$\sigma_t^{\text{res}} = \sigma_t^{\text{bin}} - \overline{\sigma_t}.$$

Before applying an OA to the residual density field, we seek to remove the influence of high-frequency tidal motions. Temperature data at all three depths from the mooring located at 37.82°N, 125.85°W show strong semidiurnal variations due to internal tides during the period of SS1 (T. Chereskin 1997, personal communication). The continuous nature of sampling using SeaSoar aliases this tidal signal into apparent spatial variability. If possible, it is desirable to remove this tidal signal. Fortunately, two independent records of the time-dependent temperature fields exist from which to estimate the tidal variability (mooring and SeaSoar). Although the internal tide may vary spatially and temporally, we assume that the tidal signal does not vary significantly over the 70 km by 100 km study region and 2.5 days it took to perform the survey.

The phase and amplitude of the M_2 tidal constituent (period 12.42 h) are calculated by least squares fit to the mooring temperature data at 150 and 300 m between 28 June and 4 July. The same fit is applied to the SS1 SeaSoar temperature data. The results of both fits are shown in Table 1. The amplitudes agree quite well and the phases are in approximate agreement. The agreement in phase and amplitude, estimated from the mooring (a point measurement) and from the SeaSoar (an area measurement), supports the assumption that the internal tidal signal does not vary significantly over the SS1 region.

Assuming that the mooring data most closely resemble the actual tidal signal and that the agreement between mooring and SeaSoar-derived tidal signals corroborates the ability of SeaSoar to measure the actual tidal variability, an M_2 tidal constituent is fit to the SeaSoar residual density data in each 10-m vertical bin. Since the mean field has (by definition) no temporal

variability, the residual density field is used to fit the tidal signal. Otherwise, there is a risk of aliasing the spatial variability of the time-independent mean into temporal variability. To compute the detided residual, the fitted tidal signal is subtracted from the residual density data. Again, the tidal signal being removed is assumed to be spatially invariant, although the ambient stratification varies over the study region.

Next, the detided residual field is interpolated onto a regular grid using standard OA. Objective analysis requires the specification of a spatial correlation function (see the appendix). The decay scale a and zero crossing $b/2$ that result from fitting the correlation function (A1) to the actual density correlation data vary slightly with depth. The minimum, mean, and maximum values for the correlation parameters are shown in Table A1. The mean decay scale is 22.0 km and the mean zero crossing $b/2$ is 20.6 km. The OA is carried out using the fitted values of a and b at each vertical level. For comparison, recent studies that have applied OA to density (or dynamic height) data from the CCS (e.g., Kosro et al. 1991; Walstad et al. 1991) obtain a decay scale of 50 km and a zero crossing of approximately 60 km. Due to the increased sampling resolution of our survey compared with previous surveys and the careful removal of the large-scale mean, we can apply the OA with smaller length scales.

The detided residual data are interpolated onto a uniform 2-km grid that has 75 points in the x direction and 53 points in the y direction. Since the residual data are gridded onto an area that extends approximately 15 km beyond the region where measurements were taken, some extrapolation takes place. The OA allows for the computation of the rms error expected at an objectively analyzed point. This rms error is expressed in the form of ''error maps'' (Bretherton et al. 1976), which are the ratio of the error variance to the data variance. For the purpose of this analysis, we will refer to this error estimate as the ''error covariance.'' None of the gridded data with an error covariance greater than 0.1 (10% of the data variance) is used in the subsequent diagnosis of vertical velocity. The objectively analyzed, detided residual density field is shown in Fig. 4c. Finally, the total density field (Fig. 4d) is computed by adding the objectively analyzed residual data to the mean field.

The gridded three-dimensional density field reproduces the primary features seen in the raw data (cf. Figs. 2b and 4d). The curved front that strengthens as it nears the eastern edge of the survey region, as well as the closed density contours (e.g., σ_t = 26.2 kg m^{-3}) that correspond to the location of the cyclonic eddy, are evident in both the maps of raw and gridded density data (Figs. 2b and 4d). Also, vertical sections of the gridded density field (e.g., from lines 4, 5, and 6 along 37.87, 37.78, and 37.69°N shown in Fig. 5) show the primary features seen in the raw data: sloping isopycnals on the east and west ends of the sections (corresponding to the location of the geostrophic jet) and domed isopycnals in the middle of the region (corresponding to the location of the cyclonic eddy). The gridded density field also reproduces several of the resolved smaller-scale features. In the horizontal plane, these secondary features are O(10–20 km) meanders of the density front, and in the vertical plane the secondary features are variations in isopycnal thickness with a similar O(10–20 km) horizontal length scale. This is shown particularly well on lines 4 and 5 at about 126.5°W and 100 m (cf. Figs. 3a,b and 5a,b). Finally, direct comparisons of the bin-averaged and gridded density data were made. The

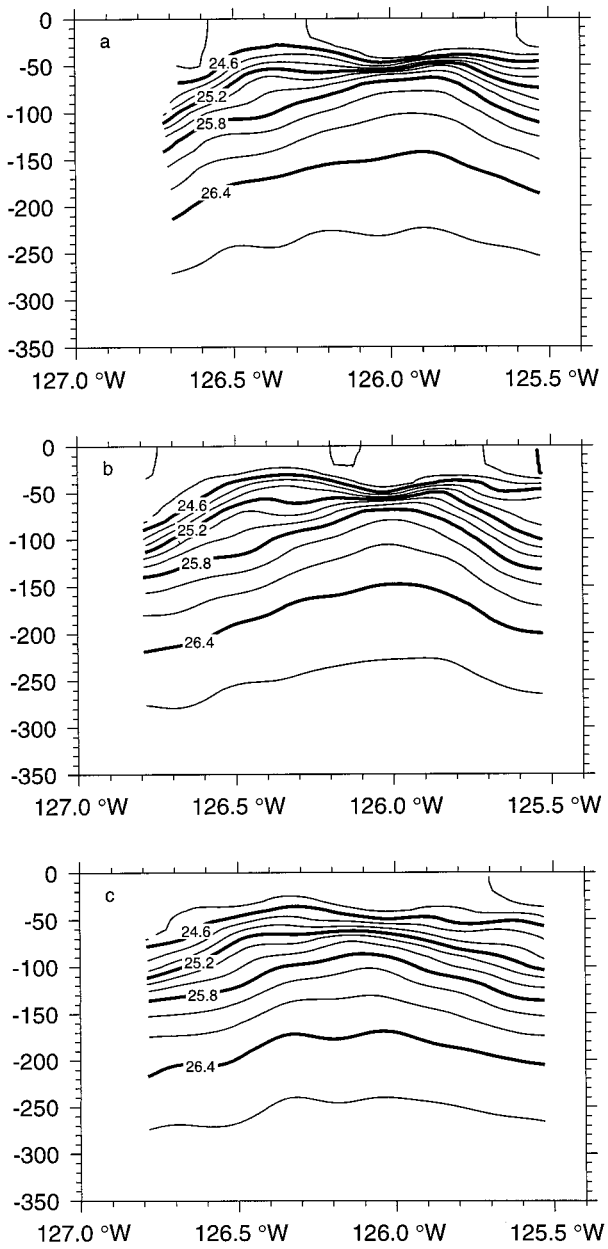

FIG. 5. Vertical sections of the total interpolated density (kg m^{-3}) field along (a) line 4, 37.87°N; (b) line 5, 37.78°N; and (c) line 6, 37.69°N.

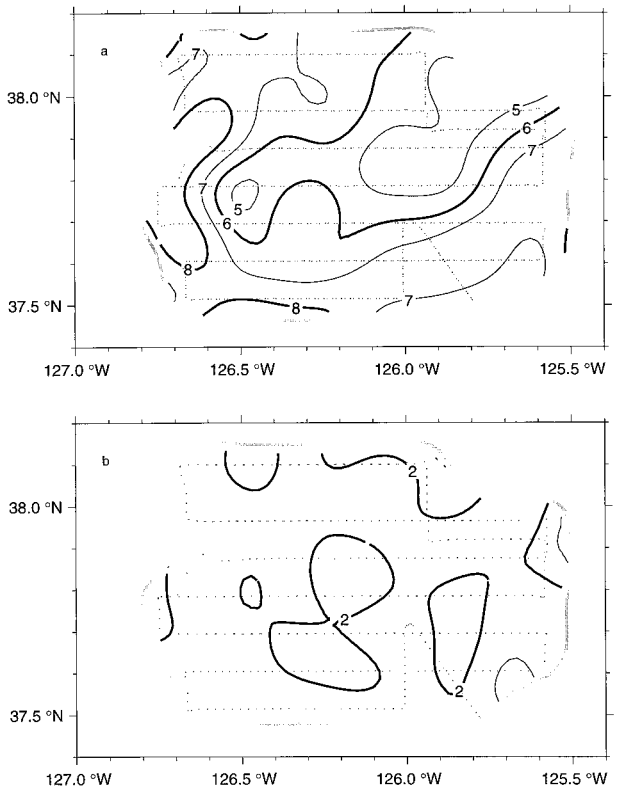

FIG. 6. Maps of buoyancy frequency N in cycles per hour calculated from the gridded density field at depths of (a) 100 m and (b) 300 m.

rms difference calculated over the entire volume is 0.08 kg m^{-3}. The mean square difference calculated over the entire volume is 0.9% of the data variance.

The horizontal distribution of buoyancy frequency, calculated from the gridded density data, is shown in Fig. 6. At 100 m, the stratification is stronger within the jet (8 cph) than within the eddy (4–5 cph). At 300 m, the entire region is almost homogeneously weakly stratified (2 cph). The vertical sections of density, both the raw (Fig. 3) and the gridded (Fig. 5), show that regions of strongest stratification with values greater than 10 cph overlay the cyclonic eddy. The region of high stratification separates the top surface of the cyclone from the surface mixed layer at a depth of approximately 50 m.

b. ADCP data

In order to obtain a nondivergent velocity field that can be used as a reference for calculating absolute geostrophic velocity, the shipboard ADCP data are processed in a similar fashion to that used for the density data. A nondivergent mean field that best fits the observations is identified, then a residual velocity field is calculated by subtracting the nondivergent mean field from the raw data. This residual field may be divergent. A gridded nondivergent streamfunction is calculated from the residual velocity field using objective analysis for vector variables, following Bretherton et al. (1976) and Walstad et al. (1991). Finally, the streamfunction that corresponds to the mean field is added to the residual streamfunction to produce the total interpolated nondivergent velocity field streamfunction.

We choose a first-order polynomial to describe the mean nondivergent velocity field. Given the choice of a paraboloid for the mean density field (1), a planar velocity field is consistent with geostrophy. The streamfunction that corresponds to the planar mean nondivergent velocity field is parabolic. If the mean streamfunction, signified by an overbar, is described by a second-order polynomial similar to the paraboloid describing the mean density field (1),

$$\overline{\psi} = \hat{A}x^2 + \hat{B}xy + \hat{C}y^2 + \hat{D}x + \hat{E}y + \hat{F}, \qquad (2)$$

then the mean nondivergent velocity fields are

$$\overline{u}_{\mathrm{nd}} = -\frac{\partial \psi}{\partial y} = -2\hat{C}y - \hat{B}x - \hat{E} \qquad (3a)$$

and

$$\overline{v}_{\mathrm{nd}} = \frac{\partial \psi}{\partial x} = 2\hat{A}x + \hat{B}y + \hat{D}. \qquad (3b)$$

The values of $\hat{A}$, $\hat{B}$, $\hat{C}$, $\hat{D}$, and $\hat{E}$ are determined by a least squares fit of (3a) and (3b) to the raw ADCP data; $\hat{F}$ is arbitrary and set to zero. The raw ADCP velocity vectors at a depth of 200 m are shown in Fig. 7a and the streamfunction $\overline{\psi}$ that corresponds to the mean nondivergent velocity field is shown in Fig. 7b.

The residual velocity field, calculated by taking the difference between the mean nondivergent velocity field and the raw ADCP data, now contains any divergence that was originally in the raw data. Next, we perform the OA, following an application by Walstad et al. (1991), to determine the residual nondivergent velocity field. The residual density field correlation function (A1) with the fitted length scales is used to determine the longitudinal and transverse correlation functions [Eqs. (A2) and (A3), respectively] for the nondivergent velocity field. The results of the objective analysis on the residual ADCP data at 200 m are shown in Fig. 7c, again restricting the results to regions where the OA error covariance is less than 0.1. The final interpolated nondivergent streamfunction (Fig. 7d) is computed by adding the mean streamfunction (2) to the interpolated residual field streamfunction. At 200 m, the flow field is dominated by southwestward flow in the northwest and northeastward flow in the southeast. The cyclone/jet feature evidently tilts with depth (cf. Fig. 4d). Finally, direct comparisons were made between the raw ADCP velocities and the gridded, nondivergent velocity field. The rms difference in the u component (east–west) was 0.054 m s^{-1} and the rms difference in the v component (north–south) was 0.062 m s^{-1}.

In the data reduction process, the SeaSoar density and

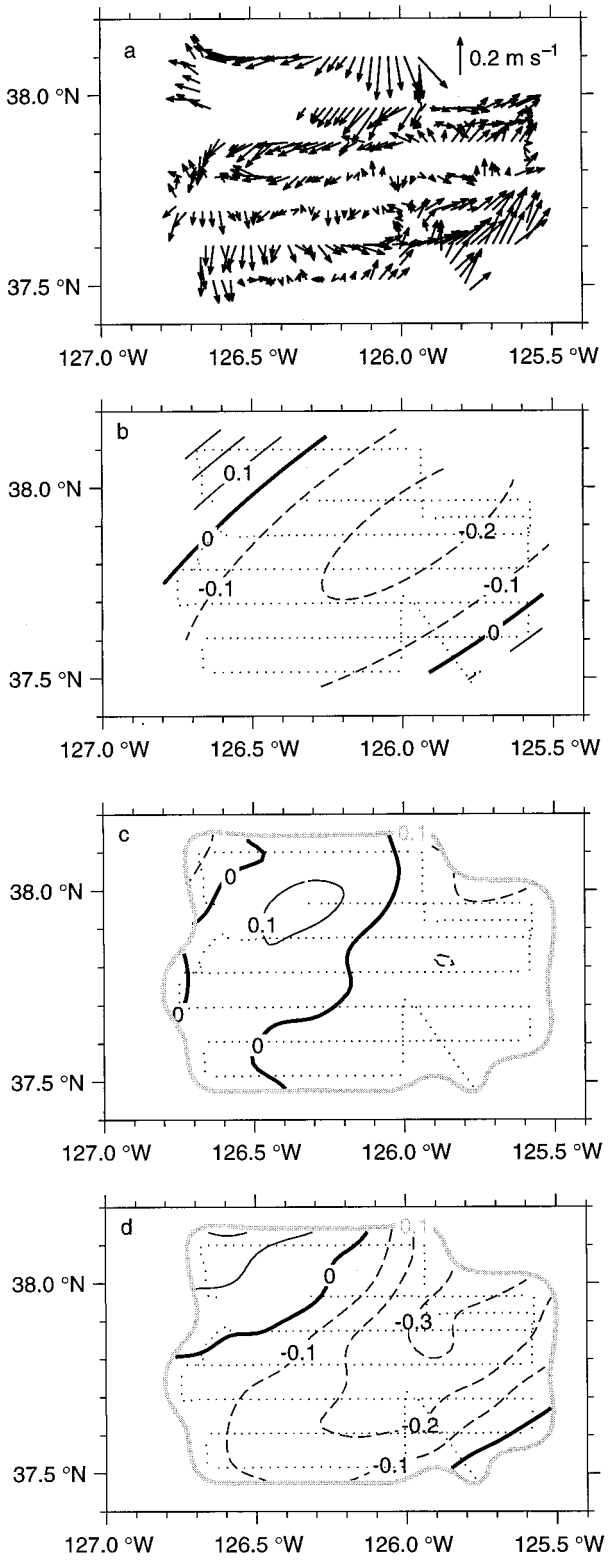

FIG. 7. Data reduction process for ADCP data at 200 m: (a) raw ADCP velocity vectors, (b) fitted nondivergent mean streamfunction ($m^2\ s^{-2}$), (c) objectively analyzed residual streamfunction, and (d) total interpolated streamfunction. The streamfunctions as shown have been scaled by f and are equivalent to dynamic height. The bottom two panels also show the 0.1 error covariance contour.

ADCP data are treated as synoptic. In reality, the survey took 60 hours (2.5 days) to complete; therefore, the issue of temporal variability and its influence upon the objectively analyzed fields needs to be addressed. The treatment of high-frequency internal tides has already been discussed. Kosro et al. (1994) traced the path of the cyclonic eddy at the focus of SS1, using satellite SST images, over the period from April through July 1993 and found that the cyclone translated WSW at an average speed of 0.05 m s^{-1}. At this speed, the cyclone would translate approximately 10 km over 2.5 days. While translation of the eddy will affect the synopticity of the objectively analyzed fields, the influence will be small considering the length scales over which the gridded data are smoothed. Also, the observed decorrelation timescales for temperature and velocity are between 2 and 3 days, as determined by the first zero-crossing of the autocorrelation of temperature and velocity computed from the time series of mooring data at 150 m.

4. Geostrophic velocity

The absolute geostrophic velocity is calculated from the gridded three-dimensional density and ADCP fields. We begin by calculating the geostrophic shear from the gridded density field, via the thermal wind relation

$$\rho_0 f \frac{\partial u_g}{\partial z} = g \frac{\partial \rho}{\partial y}, \tag{4a}$$

$$\rho_0 f \frac{\partial v_g}{\partial z} = -g \frac{\partial \rho}{\partial x}, \tag{4b}$$

where ρ_0 is the average density over the entire volume, f is the local Coriolis parameter, u_g and v_g are the geostrophic velocities, and ρ is the spatially variable gridded density field. Calculations involving spatial derivatives of gridded fields use centered finite differences on interior points and forward or backward differences on boundary points. The geostrophic velocity relative to 200 m is computed by vertically integrating the geostrophic shear given by (4a) and (4b) from a depth of 200 m where the geostrophic velocity is assumed to be zero (level of no motion). The geostrophic velocity field is made absolute by adding in the nondivergent ADCP reference velocity field at a depth of 200 m (level of known motion). A depth of 200 m is chosen as the reference because the signal-to-noise ratio of the geostrophic jet is largest at this depth.

In addition, we calculate the absolute dynamic height fields to enhance our visualization of the horizontal flow fields. The absolute dynamic height is calculated by integrating the specific volume anomaly (from the gridded density field) relative to 200 m, and adding in the reference ADCP streamfunction at a depth of 200 m.

The geostrophic velocity field (as depicted by the absolute dynamic height Fig. 8) shows the jet making a strong cyclonic meander and some recirculation within the cyclonic eddy. The maximum geostrophic velocity

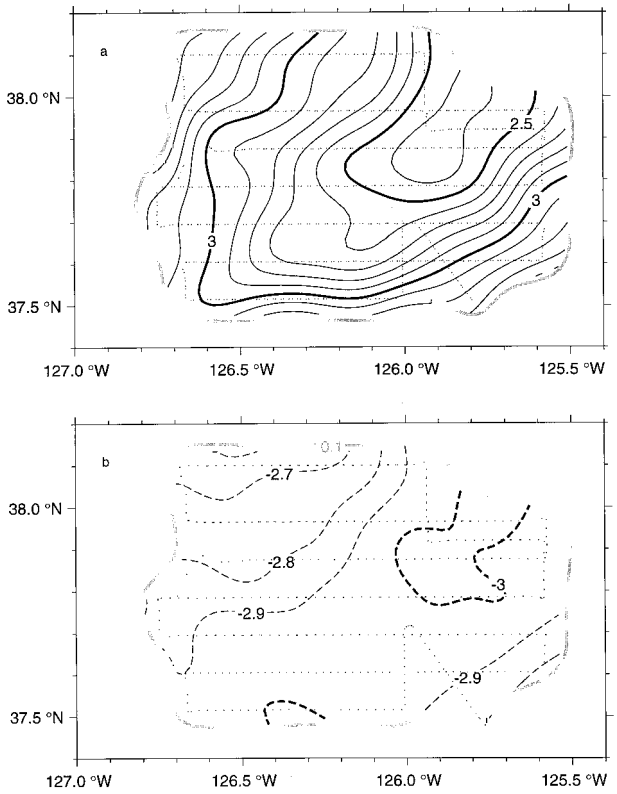

FIG. 8. Absolute dynamic height ($m^2\ s^{-2}$) at (a) 100 m and (b) 300 m. Dynamic height relative to 200 m is calculated from the gridded density field and then referenced to the gridded ADCP data at that depth to produce the absolute dynamic height field.

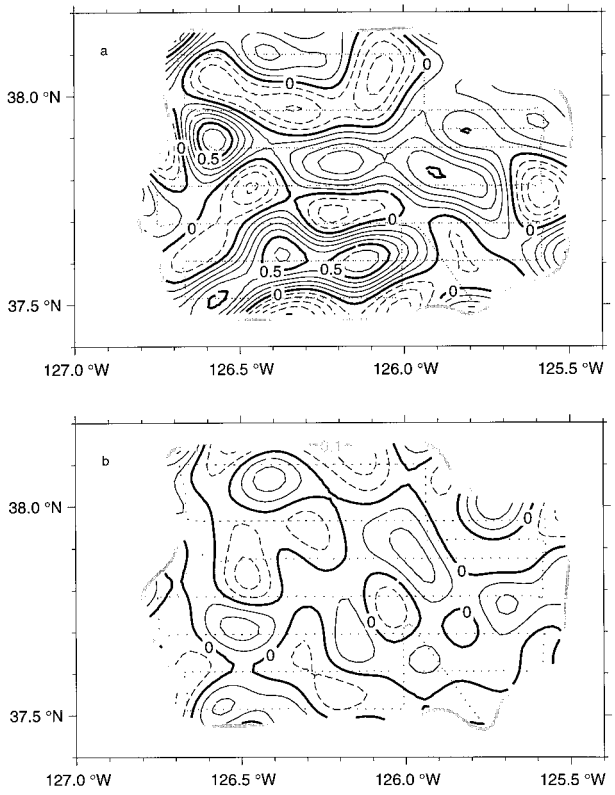

FIG. 9. Maps of scaled relative vorticity ζ_g/f calculated from the geostrophic velocity at (a) 100 m and (b) 300 m. Relative vorticity ranges from $-0.4f$ to $+0.6f$ at 100 m, and from $-0.3f$ to $+0.3f$ at 300 m.

is 0.9 m s^{-1} and occurs within the jet above 25 m. In general, the jet gains speed as the density front strengthens near the southern and eastern boundaries. The absolute geostrophic velocities are strongest in the upper 50 m and weaken consistently below 100 m. At 100 m, the jet meanders over length scales of 20–30 km. There are particularly strong short-scale cyclonic meanders located along the western edge of the region (126.5°W) near 37.85° and 37.5°N (see Fig. 8). At 300 m, the jet is still noticeable especially in the northern part of the region where the jet enters, and there is still evidence of weak cyclonic circulation centered near 37.8°N, 126.0°W (see Fig. 8b).

As mentioned before, the center of the entire cyclonic feature shifts to the southwest as depth increases (cf. Figs. 8a, 7d, and 8b). This implies a tilting of the of the cyclone and jet. On the broader length scale, the jet meander and cyclone are representative of a single streamfunction trough, and the position shift with depth represents a phase lag between the trough location at one depth versus the trough location at another. According to baroclinic instability theory, troughs in the streamfunction pattern near the surface should lag deeper troughs along the direction of the mean flow (Pedlosky 1987). This is consistent with our observations (i.e., Figs. 8a, 7d, and 8b).

The relative vorticity field,

$$\zeta_g = \frac{\partial v_g}{\partial x} - \frac{\partial u_g}{\partial y},$$

was calculated from the absolute geostrophic velocity. The relative vorticity field scaled by f at a depth of 100 m is shown in Fig. 9a. The relative vorticity at this depth ranges from $-0.4f$ to $0.6f$. At shallower depths, relative vorticities increase, exceeding $+1.0f$ in some locations well away from the boundary. The main features seen in the map of ζ_g are the strong cyclonic center at 37.8°N, 125.9°W corresponding to the eddy, surrounded by patches of varying positive and negative relative vorticity. Comparing the location of these patches to the small-scale curvature in the density front shows that local minima and maxima in the relative vorticity field coincide with strong curvature in the density front. These patches of ζ_g are approximately 20–30 km across. There is also evidence of the shear vorticity within the jet. Although the pattern is somewhat confused by the presence of such strong curvature vorticity, there is a tendency for anticyclonic relative vorticity to ring the cyclonic relative vorticity. This is most easily seen in

the southern and southeastern portions of the survey region where the jet runs mainly east–west (see Fig. 9a).

The relative vorticity at 300 m (Fig. 9b) shows similar patterns, although reduced in magnitude (anticyclonic and cyclonic maxima of $-0.3f$ and $0.3f$), as the relative vorticity at 100 m. There is considerable vertical coherence in the relative vorticity field. Also, the pattern consistent with shear vorticity within the jet is apparent at 300 m along the northern, western, and southern edges of the SS1 region.

The geostrophic velocity and relative vorticity are large within this feature. The Rossby number (given by the ratio of geostrophic relative vorticity to f) is also large with a maximum of 0.6 at 100 m and exceeding 1.0 near the surface. In high Rossby number flows with strong curvature in the streamfunction field, the primary force balance will shift from thermal wind to gradient wind. In a low pressure cyclone with strong curvature the velocity field in thermal wind balance will be stronger than the velocity field in gradient wind balance. A direct comparison between the absolute geostrophic velocity field and the objectively analyzed, nondivergent ADCP velocity field shows the geostrophic field to be consistently stronger. The largest difference (0.60 m s^{-1}) is observed at a depth of 30 m near 37.5°N, 126.4°W, which corresponds visually to the location of maximum curvature in the dynamic height field. The difference between the gridded ADCP velocity field and geostrophic velocity field is consistent with the gradient wind balance. The inclusion of gradient wind balance will be addressed in a future paper aimed at making higher-order (in Rossby number) estimates of the three-dimensional circulation.

5. Vertical velocity

Vertical velocities are calculated using the Q-vector form of the QG omega equation. The Q-vector equation is derived from the QG momentum and the adiabatic density equations. By separating the total horizontal velocity field (u, v) into a geostrophic component (u_g, v_g) and an order Rossby number (ε)—assumed to be small $(\varepsilon \ll 1)$—ageostrophic component (u_a, v_a), the QG momentum equations and adiabatic density equation may be written as

$$\frac{D_g u_g}{Dt} - fv_a = 0, \tag{5a}$$

$$\frac{D_g v_g}{Dt} + fu_a = 0, \tag{5b}$$

and

$$\frac{D_g \rho}{Dt} + w\frac{\partial \rho}{\partial z} = 0, \tag{6}$$

where

$$\frac{D_g}{Dt} = \frac{\partial}{\partial t} + u_g\frac{\partial}{\partial x} + v_g\frac{\partial}{\partial y}.$$

Using the hydrostatic relation,

$$\frac{\partial p}{\partial z} = -\rho g, \tag{7}$$

the density equation (6) can be rewritten as

$$\frac{1}{\rho_0}\frac{D_g}{Dt}\frac{\partial p}{\partial z} + N^2 w = 0, \tag{8}$$

where N is the buoyancy frequency

$$N^2 = -\frac{g}{\rho_0}\frac{\partial \rho}{\partial z}.$$

We have retained the horizontal variability of N in (8). This is formally inconsistent with the QG approximation (see Pedlosky 1987). By writing the total density as

$$\rho(x, y, z, t) = \rho_0 + \overline{\rho}(z) + \rho'(x, y, z, t),$$

where ρ_0 is a constant, $\overline{\rho}$ is the background density profile in the absence of motion and ρ' is the departure from that background, and nondimensionalizing under geostrophic scaling assumptions (thermal wind as the primary balance), the ratio of ρ' to $\overline{\rho}$ is

$$\frac{\rho'}{\overline{\rho}} = \frac{O\left(\dfrac{fLU}{g'H}\right)}{O(1)} = \frac{O(\varepsilon F)}{O(1)},$$

where ε is the Rossby number

$$\varepsilon = \frac{U}{fL},$$

F is the internal Froude number

$$F = \frac{f^2L^2}{g'H},$$

the characteristic horizontal length scale is L, and H is the characteristic thickness of a density layer. Thus, retaining the horizontal variability of N treats terms of $O(\varepsilon F)$ as $O(1)$. The values of relative vorticity within the SS1 region (see Fig. 9) certainly indicate that Rossby numbers approaching $O(1)$ are possible. The Froude number F can be rewritten as the inverse Burger number, or the square of the ratio of the geometric length scale (L) to the baroclinic deformation radius (L_R)

$$F = \frac{L^2}{L_R^2}.$$

The primary length scale of variability within the density field (Fig. 4d) and the absolute dynamic height field (Fig. 8) is determined by meanders with wavelengths of 20–30 km, and the relative vorticity field (Fig. 9) is dominated by patches that are 20–30 km in diameter. Estimates of the first baroclinic deformation radius for

the CCS are between 20 and 30 km (Chelton et al. 1998). Therefore, F may be $O(1)$ as well as ε. A future study will examine the consequences of including higher-order terms consistently to obtain a diagnostic equation for w.

The geostrophic relation

$$fu_g = -\frac{1}{\rho_0}\frac{\partial p}{\partial y}, \tag{9a}$$

$$f\upsilon_g = \frac{1}{\rho_0}\frac{\partial p}{\partial x} \tag{9b}$$

is then used to remove the time derivatives among (5a), (5b), and (8) to obtain the diagnostic relationship

$$\frac{\partial}{\partial x}(N^2 w) - f^2\frac{\partial u_a}{\partial z} = 2f\left(\frac{\partial \upsilon_g}{\partial x}\frac{\partial u_g}{\partial z} + \frac{\partial \upsilon_g}{\partial y}\frac{\partial \upsilon_g}{\partial z}\right), \tag{10a}$$

$$\frac{\partial}{\partial y}(N^2 w) - f^2\frac{\partial \upsilon_a}{\partial z} = 2f\left(\frac{\partial u_g}{\partial x}\frac{\partial u_g}{\partial z} + \frac{\partial u_g}{\partial y}\frac{\partial \upsilon_g}{\partial z}\right). \tag{10b}$$

In the formalism developed by Hoskins et al. (1978), the right-hand sides of (10a) and (10b) are defined as the components of a vector $\mathbf{Q}$. Invoking the thermal wind relation (4), horizontal derivatives of the density field can be substituted for the geostrophic shear. The vector $\mathbf{Q}$ can then be expressed in the more compact form:

$$\mathbf{Q} = 2\frac{g}{\rho_0}\left(\frac{\partial \mathbf{u}_g}{\partial x}\cdot\nabla\rho, \frac{\partial \mathbf{u}_g}{\partial y}\cdot\nabla\rho\right), \tag{11}$$

where ∇ is the horizontal gradient operator. Taking the divergence of the vector $\mathbf{Q}$ yields

$$\nabla^2(N^2 w) - f_0^2\frac{\partial}{\partial z}\left(\frac{\partial u_a}{\partial x} + \frac{\partial \upsilon_a}{\partial y}\right) = \nabla\cdot\mathbf{Q}. \tag{12}$$

Since all divergence is due to the ageostrophic motion in the QG approximation, the continuity equation

$$\frac{\partial u_a}{\partial x} + \frac{\partial \upsilon_a}{\partial y} + \frac{\partial w}{\partial z} = 0, \tag{13}$$

can be used to substitute the vertical derivative of w for the ageostrophic divergence in (12). This yields the final form of the Q-vector equation

$$\nabla^2(N^2 w) + f_0^2\frac{\partial^2 w}{\partial z^2} = \nabla\cdot\mathbf{Q}. \tag{14}$$

The Q-vector equation is a Poisson equation in three dimensions. The forcing terms and coefficients are all determined by the three-dimensional density and geostrophic velocity fields. All that is now required to solve the Q-vector equation are boundary conditions. The surface ($z = 0$ m) boundary condition,

$$w(x, y, 0) = 0, \tag{15a}$$

is set by the rigid-lid approximation consistent with quasigeostrophy. If the density data extended to the bottom ($\sim$4000 m), the boundary condition would be set by a no-normal-flow constraint

$$w(x, y, h) = -\left(u_g\frac{\partial h}{\partial x} + \upsilon_g\frac{\partial h}{\partial y}\right),$$

where h is the horizontally variable bottom depth. The SeaSoar-derived density data, however, end at 310 m. There are two possible boundary conditions at this depth: w equals zero (Dirichlet) or the first vertical derivative of w equals zero (Neumann). The choice of boundary condition is arbitrary. The Dirichlet boundary condition seems unlikely, though, considering that a depth of 310 m is within the main thermocline where there is more likely to be vertical motion rather than the complete absence of vertical motion. Therefore, we set the vertical derivative of w to zero at 310 m,

$$\frac{\partial w}{\partial z}(x, y, -310 \text{ m}) = 0. \tag{15b}$$

This assumes that the divergence at 310 m is zero, or that the flow at this depth is dominated by the geostrophic flow. A comparison of the vertical velocities diagnosed using the Dirichlet versus the Neumann bottom boundary condition reveals no qualitative change in the horizontal patterns of w. There is a quantitative change in the magnitude of the diagnosed vertical velocities, though. The difference between the vertical velocity field diagnosed using the Dirichlet versus the Neumann bottom boundary condition was ± 1 m d^{-1} at 100 m and ± 3 m d^{-1} at 200 m.

The lateral boundary conditions are also indistinct. Following Rudnick (1996), the horizontal boundaries are moved away from the region of interest. This should minimize the effects of whatever boundary conditions are used. The boundaries of the calculation extend approximately 15 km past the perimeter of the region where data were collected. The lateral boundary conditions applied are

$$\frac{\partial w}{\partial x}(x_{\text{west}}, y, z) = \frac{\partial w}{\partial x}(x_{\text{east}}, y, z) = 0, \tag{15c}$$

$$\frac{\partial w}{\partial y}(x, y_{\text{south}}, z) = \frac{\partial w}{\partial y}(x, y_{\text{north}}, z) = 0. \tag{15d}$$

To further minimize the effects of the horizontal boundaries, the divergence of $\mathbf{Q}$ is set to zero outside of the 0.1 error covariance contour (see Figs. 4d and 7d). The Q-vector equation (14) is solved using the method of successive overrelaxation with the forcing and coefficients given by the three-dimensional density and geostrophic velocity fields and the boundary conditions (15).

The diagnosed vertical velocity field has a horizontal distribution that has length scales similar to the relative vorticity. At 100 m, there are patches of upwelling and downwelling approximately 20–30 km in diameter (see Fig. 10a). However, at 300 m the horizontal distribution

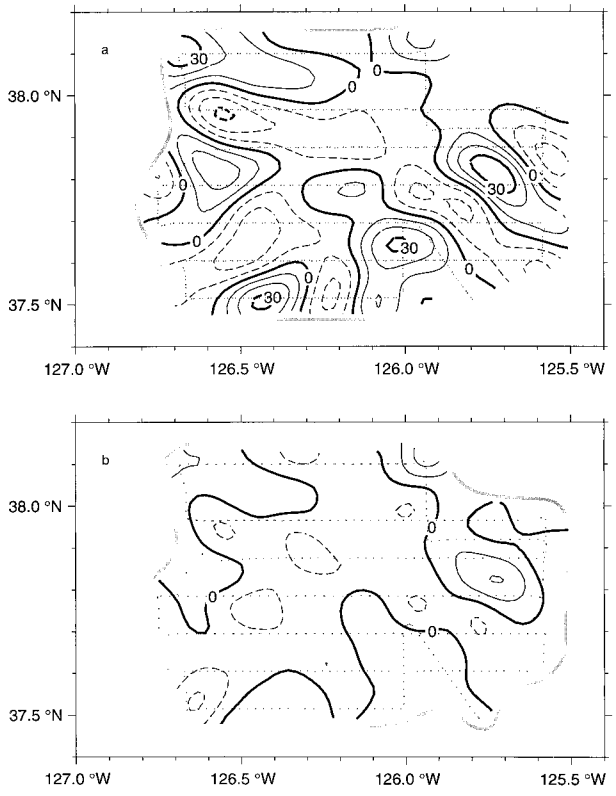

FIG. 10. Maps of vertical velocity w in m d^{-1} calculated from the gridded density and geostrophic velocity fields via the Q-vector equation at (a) 100 m and (b) 300 m. Vertical velocity ranges from −30 to 45 m d^{-1} at 100 m and from −30 to 25 m d^{-1} at 300 m.

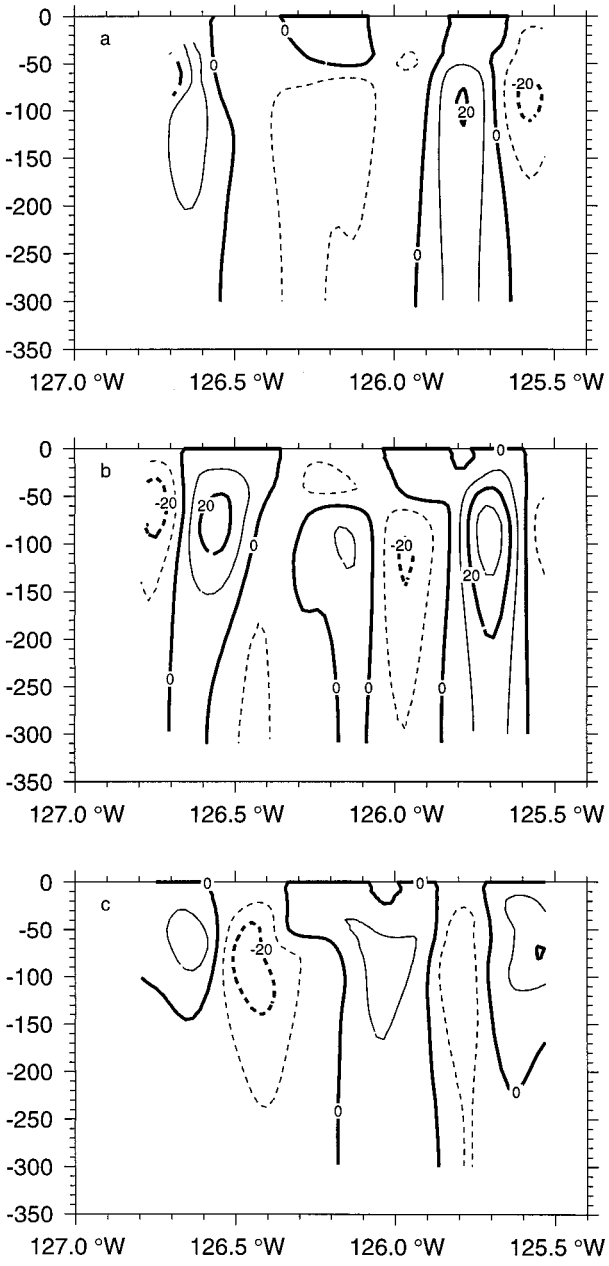

FIG. 11. Sections of vertical velocity w (m d^{-1}) along (a) line 4, 37.87°N; (b) line 5, 37.78°N; and (c) line 6, 37.69°N.

of w has a larger (~75 km) scale. This is characterized by the separation of the vertical velocity field into a large downwelling patch in the northwest and a similar sized patch of upwelling in the southeast.

The strongest vertical velocities are located within the jet. There is a weak downwelling region within the cyclonic eddy centered near 37.8°N, 126.0°W. The weak vertical velocities within the eddy are consistent with the strong stratification there (Fig. 6). Downwelling within the eddy is consistent with a low pressure cyclone. Ageostrophic pressure-driven flow would be into the eddy and then downward as a consequence of continuity and the proximity of the rigid surface. As a result of this secondary circulation, Lagrangian drifters deployed in the surface layers of the CCS may become trapped within cyclonic eddies.

Patches of alternating positive and negative w are aligned in series along the jet. These patches are located in the vicinity of small-scale curvature in the density front and absolute dynamic height field (see Fig. 8). The maximum vertical velocity is O(40 m d^{-1}) for both upwelling and downwelling, and occurs at a depth between 70 and 100 m (Fig. 11). The density field exhibits the strongest horizontal gradients between these depths, so forcing of the Q-vector equation is likely to be strong as well.

At 300 m, the vertical velocity field is weaker (see Fig. 10b), but the patterns have remained coherent. At this depth, features with a broader length scale are more apparent: downwelling upstream and upwelling downstream of the sharp cyclonic bend in the density front. The pattern is also observable at 100 m (Fig. 10a) but is disrupted by the strong upwelling region at the western end of line 5 (37.78°N).

The vertical distribution of w is generally of one sign between the surface and 310 m with a maximum occurring between 70 and 100 m (Fig. 11). In certain

places, though, the vertical distribution of w is baroclinic (e.g., at 126.25°W in Fig. 11c). This occurs outside of the jet in regions of weaker vertical velocity, and the sign change occurs at approximately 50 m, near the base of the surface mixed layer (see Fig. 11). At the base of the mixed layer, particularly above the cyclonic eddy at 126.0°W along line 5 (37.78°N), the stratification is strong, and the location of the strong stratification coincides with the change in vertical velocity. This can be seen by comparing the vertical sections of raw density with N overlain (Fig. 3) and vertical sections of w (Fig. 11).

6. Discussion

The fine resolution of SeaSoar density and ADCP velocity measurements during SS1 allow for an unprecedented view of the physical characteristics of the meandering jet and adjacent cyclone. Previous observations of the horizontal velocities within similar jets in the CCS are comparable to those observed here with speeds of 0.8–1.0 m s^{-1} (Kosro and Huyer 1986; Rienecker and Mooers 1989; Kosro et al. 1991; Huyer et al. 1998). Estimates of in situ relative vorticity within the CCS are few. In one study (Paduan and Niiler 1990), relative vorticity is determined from clusters of drifters. In two other studies (Kosro and Huyer 1986; Dewey et al. 1991), high-resolution ADCP transects are used to estimate the shear vorticity within oceanic jets. Vertical motion has previously been inferred from tracers (Flament et al. 1985; Kadko et al. 1991; Washburn et al. 1991) or modeling studies (Haidvogel et al. 1991), with which we further compare our results below. Chumbinho (1994) estimated vertical velocities associated with the SS1 cyclone in May 1993 (when it was located inshore near Point Arena) using a digital filtering technique applied to a primitive equation model that was initialized with density data from a standard CTD survey. That study had relatively coarse spacing between the CTD stations (10 km or more).

The diagnosis of vertical velocity here shows strong vertical velocities associated with this meandering jet and adjacent cyclone. How would a water parcel moving through this region be affected by the vertical velocity field? Comparing the geostrophic velocity (Fig. 8) and vertical velocity (Fig. 10) fields gives a rough idea of the three-dimensional circulation. As fluid moves through the region advecting with the geostrophic velocity, it encounters the 20–30 km patches of vertical velocity and subsequently advects up or down.

To examine this behavior more closely, we follow the variation of w along geostrophic streamlines. A map of absolute dynamic height contours at a depth of 100 m is shown in Fig. 12a with the trajectory of a water parcel following a geostrophic streamline indicated by the heavy line. The water parcel was released at 38.12°N, 126.03°W. The geostrophic trajectory was determined by linearly interpolating the geostrophic velocity to the location of the water parcel and integrating, using a time step of 0.02 days (approximately 0.5 h), to find the water parcel's next location. The local relative vorticity and vertical velocity were also determined by interpolation and recorded as a function of time and distance traveled along the streamline.

The chosen streamline lies nearly in the center of the jet and passes through several regions of strong vertical velocity (both upwelling and downwelling). The variation of relative vorticity and vertical velocity versus distance traveled along the streamline is shown in Fig. 12b. The water parcel moving along the streamline passes through small regions where vertical velocity and relative vorticity reach local minima and maxima. Peaks in the relative vorticity field are followed immediately by peaks in the vertical velocity field. This is an indication of potential vorticity conservation. A water parcel moving with the geostrophic velocity is advected into regions where relative vorticity is at a local maximum or minimum. These regions of relative vorticity are associated with strong curvature in the density front. As the water parcel moves past a local maximum/minimum in relative vorticity, it enters a region where relative vorticity is changing rapidly. In order to conserve potential vorticity, a water parcel must either stretch or compress, which requires vertical motion.

The net vertical displacement of a parcel of water, starting from the northern end of the chosen streamline as it moves through the region, is shown in Fig. 12c. This particular water parcel trajectory was chosen because it lies nearly at the center of the jet. The net vertical displacement is calculated by integrating the water parcel's vertical velocity along the geostrophic trajectory. For the purpose of determining local values of geostrophic velocity, relative vorticity, and vertical velocity the water parcel is not allowed to change its vertical position. This constraint is strictly in keeping with the concept of following a geostrophic streamline, and it is consistent with the QG assumption that the range of vertical displacement is much smaller than horizontal displacement. By constraining the water parcel to remain at a constant depth level, we avoid mixing differently ordered terms in the QG approximation. To correctly represent the full three-dimensional pathway, not only would the vertical velocity need to be considered, but also the order Rossby number horizontal ageostrophic velocity.

Combining the information in Figs. 12a and 12c completes the picture of the overall three-dimensional circulation. The water parcel initially sinks approximately 40 m in four days, then moves into a region where it experiences relatively no vertical displacement. Over the last three days the water parcel upwells approximately 25 m. Net vertical displacement obtained by fitting a least squares line to the time-dependent displacements are 20–30 m over 2–3 days, resulting in net vertical velocities (the slope of the least squares line) of 7–15 m d^{-1} (Fig. 12c).

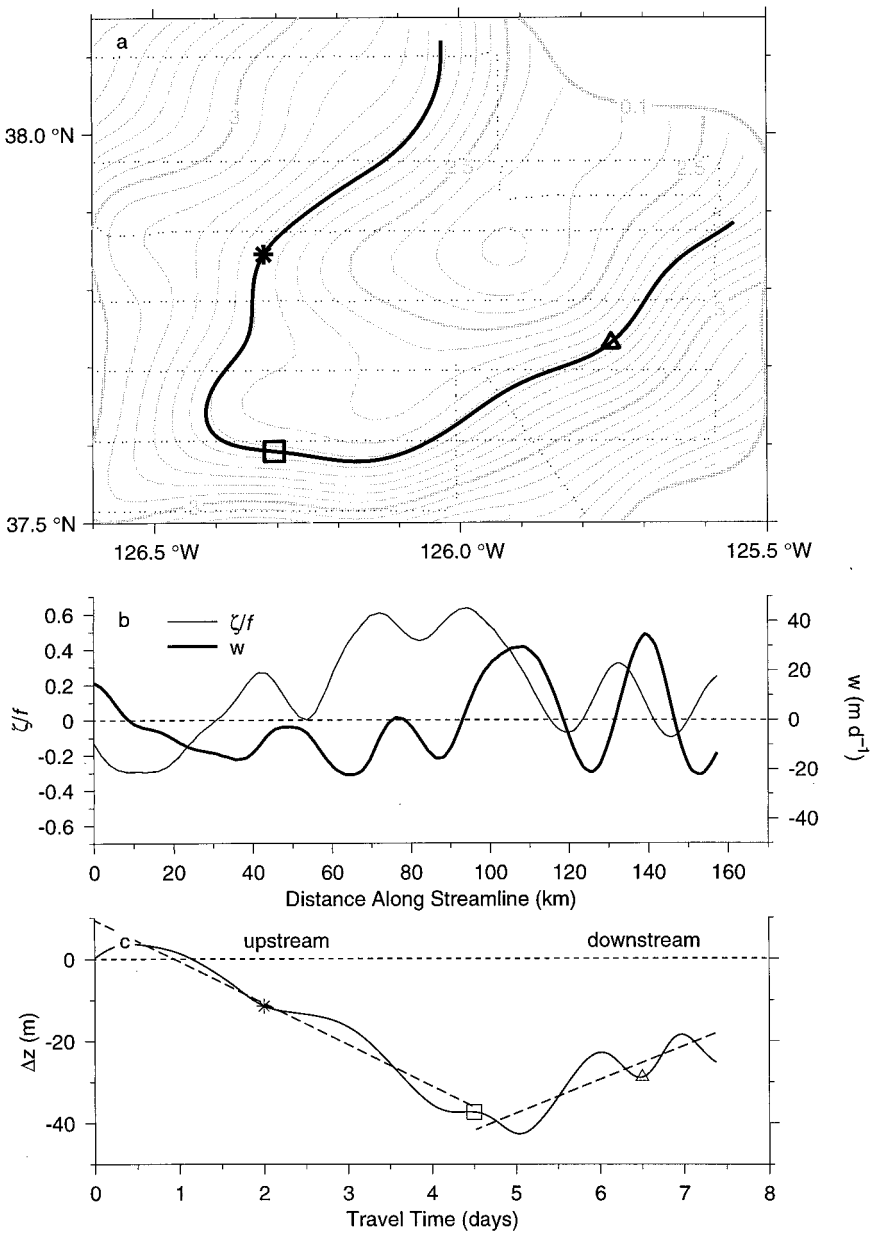

FIG. 12. (a) Water parcel trajectory (heavy line) at a depth of 100 m plotted over contours of absolute dynamic height. (b) Plots of vertical velocity w and relative vorticity ζ_g/f along the chosen geostrophic streamline. The ordinate is distance traveled along the streamline, and the values of relative vorticity relative to f are given on the left side while the values of w (m d^{-1}) are given on the right. (c) Plot of net vertical displacement as the water parcel advects along its trajectory. The ordinate is time spent traveling along the streamline.

At a depth of 100 m, geostrophic trajectories of water parcels started 5 km to the east and west of the original water parcel trajectory are analyzed in a similar fashion (Fig. 13). The original water parcel traveled roughly within the center of the jet, the parcel 5 km to the west (east) therefore lies within the jet's anticyclonic (cyclonic) flank. The vertical displacements along alternate geostrophic trajectories reinforce the previous results. Although the water parcels take different amounts of time to move through the region, their net vertical velocities remain 7–15 m d^{-1}. Likewise, the geostrophic trajectories of water parcels started at the same horizontal location, but separated by 50 m in the vertical, also have net vertical velocities of 7–15 m d^{-1}, indicated by least squares line fits (Fig. 14). Since the geostrophic jet is strongly surface intensified, the deeper water parcel moves more slowly through the region (~13 days). Thus, it spends more time within individual patches of

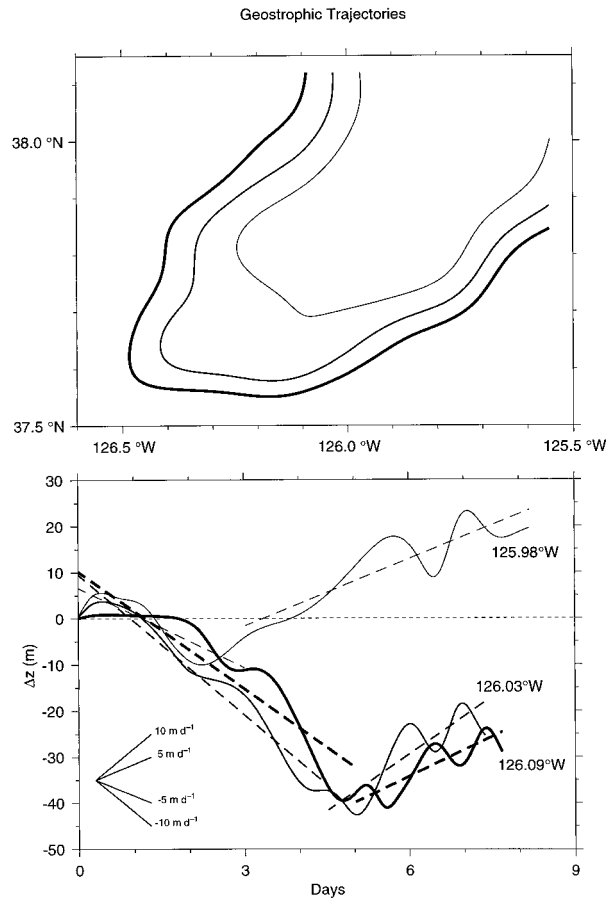

FIG. 13. Plots of geostrophic trajectories and net vertical excursions by water parcels. Three geostrophic trajectories at 100 m with their starting points separated by 5 km are shown in the upper panel. The net vertical displacements along those streamlines are shown in the lower panel. Different starting locations are indicated by line thickness. Lines fit using least squares to the upstream and downstream portions of the data are shown dashed.

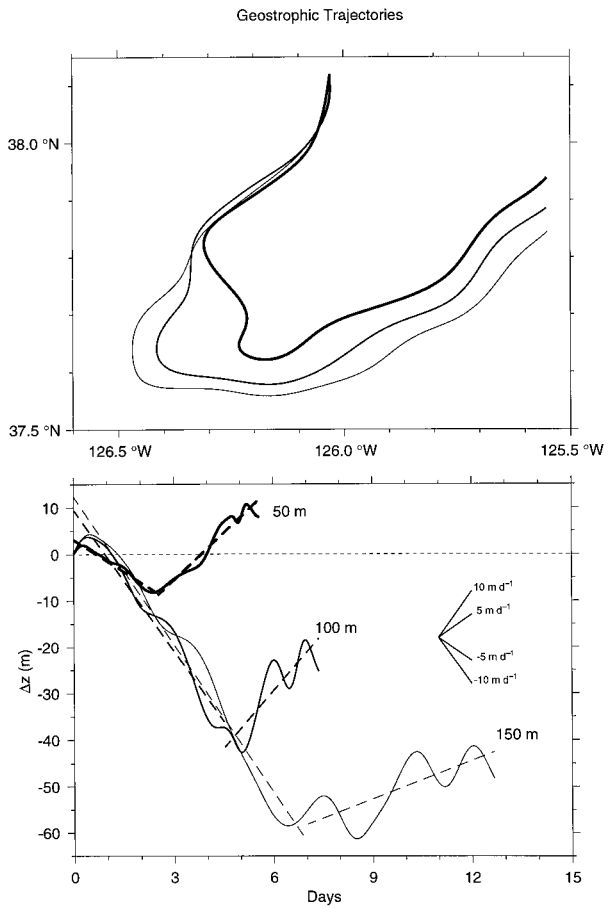

FIG. 14. Plots of geostrophic trajectories and net vertical displacements. Three geostrophic trajectories started at the same horizontal location (38.12°N, 126.03°W) but separated by 50 m in the vertical (50, 100, and 150 m) are shown in the upper panel. The net vertical excursions along those streamlines are shown in the lower panel. Different starting locations are indicated by line thickness. Lines fit using least squares to the upstream and downstream portions of the data are shown dashed.

vertical velocity and can upwell and downwell as much as 55 m in 6–7 days (Fig. 14). Conversely, the shallower water parcel undergoes less net vertical displacement because it moves through the region more quickly (~6 days).

The geostrophic trajectories of water parcels started at the same horizontal location, but separated by 50 m in the vertical, provide more evidence as to the tilting of the entire cyclone/jet feature. The geostrophic trajectories systematically shift to the southwest from 50 to 150 m (see Fig. 14 at 37.6°N, 126.4°W). This supports the evidence seen in dynamic height field (Fig. 8 and Fig. 7d).

Also apparent in Fig. 12c is the superpositioning of two different scales for vertical displacement. There is a large-scale net downwelling followed by a net upwelling that occurs over a few days, or equivalently approximately 75 km, and has an effective vertical velocity of 7–15 m d^{-1}. Superposed on this motion, though, is a much smaller scale vertical motion. These vertical motions occur over a timescale on the order of a day, or a length scale of approximately 20 km, and have strong vertical velocities (30–40 m d^{-1}). The large-scale vertical displacement is associated with the large-scale meandering of the jet. These meanders are caused by the inherent instability (baroclinic instability) of flows in thermal wind balance. Baroclinic instabilities are typified by perturbations of the flow with spatial scales of approximately 2π times the Rossby radius of deformation (about 150 km for a full wavelength, or a 75 km diameter eddy). The smaller-scale vertical motion is associated with the strong local curvature of the density front, one source of which may be small-scale frontal instability. In a linear stability analysis of a similar jet in the CCS, Barth (1994) identified two scales of baroclinic instability: traditional baroclinic instability with a length scale of $2\pi L_R$ and a frontal instability with a length scale of O(20 km). Evidence exists in our ob-

servations and derived fields for both of these length scales.

The primary timescales, determined from the net vertical motion at 100 m (Fig. 12c), are 1–2 days (short period) and 3–4 days (long period). The short period is associated with short horizontal length scales and strong vertical velocities, while the long period is associated with translation around the entire meander and weaker vertical velocities. These timescales can be compared to the decorrelation timescale from the mooring data of 2–3 days, which is associated with the approximately 10 km translation of the cyclone and jet meander over 2.5 days. The slow translation of the eddy/jet is not likely to influence the variability on either timescale. The short period variability simply happens too quickly, while the effect of translation on the long period will be to slightly alter the horizontal trajectory of a water parcel.

The primary timescales for vertical displacement can also be compared to the growth rate (approximately 1.5 days) and propagation speed (approximately 0.30 m s^{-1}) of the frontal instability in Barth (1994). The propagation speed of the frontal instability is of the same order as the horizontal advection speed of water parcels. Near the surface advection speeds are faster, at 100 m advection speeds are approximately equal to the propagation speed of the frontal instability, and deeper than 200 m advection speeds are slower. When the advection and propagation speeds are comparable, water parcels trapped in frontal instabilities may undergo greater vertical displacement, similar to the enhanced ageostrophic circulation predicted by Owens (1984).

During CTZ, a pair of studies inferred vertical motion from observations in the CCS. Kadko et al. (1991) estimate subduction rates within cold filaments of 25 m d^{-1}, using a radioactive gas tracer, as well as chlorophyll and dissolved oxygen concentrations. Washburn et al. (1991) use water mass characteristics to infer slightly smaller subduction rates of $O(10\ \text{m d}^{-1})$. Chumbinho (1994) finds maximum vertical velocities of 20–22 m d^{-1} at a depth of 100–150 m. These estimates fall within our diagnosed range of vertical velocity.

Features observed in SS1 and the modeling study by Haidvogel et al. (1991) are similar. Using a primitive equation model with a realistic coastline and bottom topography, forced by relaxing to a basic state that is a surface intensified geostrophic equatorward jet, Haidvogel et al. examined the evolution of that jet over time periods of approximately 200 days. The jet becomes unstable and forms meanders that cause the jet to move 400–500 km offshore. The jet meanders pinch off in 40–50 days usually forming a pair of eddies (cyclone and anticyclone). This temporal evolution is consistent with the evolution of the cyclone observed in SS1, which is evident in a series of SST images and ship surveys during the 1993 EBC program. For example, Kosro et al. (1994) have followed the path of this cyclonic eddy since it was first observed near Point Arena in May 1993 (Chumbinho 1994).

The values of relative vorticity and vertical velocity associated with a strong cyclonic meander from the Haidvogel et al. primitive equation model study are similar to those observed in SS1. Haidvogel et al. report vorticities of $0.8f$ and vertical velocities of 30–40 m d^{-1} at 200-m depth. The distribution of relative vorticity and vertical velocity within the filament structure are similar between the modeling study and the observations in SS1. The reported length scales of baroclinic instabilities in the model are on the order of 60–100 km (this represents a half-wavelength). This would correspond to the length scales associated with the general cyclonic curvature observed in the SS1 density data, represented by the mean field (Fig. 4b). Haidvogel et al. also report the existence of smaller scale frontal instabilities with an alongstream length scale of 30–50 km. Again, features of this length scale are directly observed in SS1.

7. Conclusions

A high-resolution SeaSoar and ADCP survey of a cyclonic jet meander and adjacent cyclonic eddy in the CCS was performed as part of the 1993 EBC project. The unprecedented resolution and synopticity of this survey provides a unique view of mesoscale features in the CCS. It allows the diagnosis of vertical velocity and, hence, a realization of the full three-dimensional circulation associated with these mesoscale features.

The SeaSoar derived density field shows a density front that has been deformed into a cyclonic meander. The density front is strongest between 70 and 100 m. The ADCP measurements show a current jet with maximum speeds above 0.5 m s^{-1} that follows the cyclonic curvature of the density front. The high-resolution of the SeaSoar and ADCP measurements make possible the application of an OA with length scales much shorter than previously used in the CCS. The mean decay scale is 22.0 km and the mean zero crossing is 20.6 km.

The geostrophic velocity fields, calculated from the objectively analyzed density data and referenced to the ADCP data at 200 m, depict a surface-intensified jet with top speeds of 0.8–1.0 m s^{-1} and a cyclonic eddy with closed circulation. The entire eddy/jet feature is tilted with the center of the feature shifting to the southwest with depth. The relative vorticity field ranges from $-0.8f$ to $+1.2f$ with the maxima occurring near the surface and is characterized by length scales of 20–30 km. Relative vorticity varies most strongly within the jet.

The objectively analyzed density and ADCP data are used to diagnose the vertical velocity field via the Q-vector form of the QG omega equation. The maximum vertical velocities are 40–45 m d^{-1} for both upwelling and downwelling and occurred at depths between 70 and 100 m. The strongest variations of vertical velocity

are within the jet and the area within the cyclone is weakly downwelling, consistent with the inferred ageostrophic circulation surrounding a low pressure cyclone. At 100 m, the diagnosed vertical velocity field is dominated by horizontal length scales of 20–30 km, but at deeper levels an underlying larger (~75 km) characteristic length scale becomes apparent. The two length scales are consistent with frontal instabilities [length scale of O(20 km)] and standard baroclinic instabilities (eddy length scale ~75 km).

Analysis of vertical motion along geostrophic streamlines indicates that net vertical excursions by water parcels advecting with the geostrophic flow are on the order of 20–30 m over 2–3 days. This corresponds to net vertical velocities of 7–15 m d^{-1}. The behavior of relative vorticity and vertical velocity along a streamline indicate that this vertical motion is being induced by potential vorticity conservation driven by changes in the relative vorticity.

Acknowledgments. We would like to thank the *Wecoma*'s Marine Technicians (Marc Willis, Brian Wendler, Mike Hill, and Tim Holt) for their tireless efforts in maintaining and operating the SeaSoar instrument. We would also like to thank the officers and crew of the R/V *Wecoma* for their skill and expertise in handling the ship under difficult weather conditions. We are very grateful to Bob O'Malley and Jane Fleischbein for administering to the shipboard computer system and for the processing, analyzing, and archiving of the data from a variety of instruments. We appreciate the assistance provided by colleagues Teri Chereskin and Peter Niiler for supplying the mooring data, and Ted Strub and Corinne James for supplying SST imagery. We also thank John Allen, Bob Haney, Jane Huyer, and Bob Smith for sharing their insight and experience during discussions of the research. This work was supported by the Office of Naval Research through Grants N00014-92J1348, N00014-91J1242, and by an AASERT Grant N00014-93-1-0730.

APPENDIX

Estimating the Correlation Function

The objective analyses of the density and ADCP data require the specification of a data correlation function and an estimate of the variance of random measurement noise. In this application we use an isotropic density correlation function of the form

$$F(r) = C_{\sigma\sigma} = \exp\left(-\frac{r^2}{a^2}\right)\cos\left(\frac{\pi r}{b}\right), \qquad \text{(A1)}$$

where r is the separation distance, and we assume that the variance of the random measurement noise is 10% of the variance of the measured data. This particular correlation function has been used to perform similar analyses in the CCS (Denman and Freeland 1985; Huyer and Kosro 1987). In order to determine the most appropriate values of the decay scale a and the zero crossing $b/2$, we calculate the spatial correlation of the σ_t^{bin} data at each vertical level, and then fit the correlation function (A1) using least squares. Spatial correlations calculated from the density data use bins 4 km wide, centered on 2, 6, 10, . . . , 126 km. The depth-averaged spatial correlation calculated from the bin-averaged σ_t data, the estimated mean σ_t field, and the residual σ_t field are shown in Fig. A1. A comparison of the three correlation curves demonstrates how important it is to remove the spatially variable mean field. The correlation behaviors of the bin-averaged raw data and mean field are quite similar; the correlation behavior of the residual data is distinctly different. The decay scale and zero-crossing for the residual field are clearly smaller than those of the mean field or bin-averaged data. This emphasizes the need to remove the spatially variable mean field before applying the objective analysis.

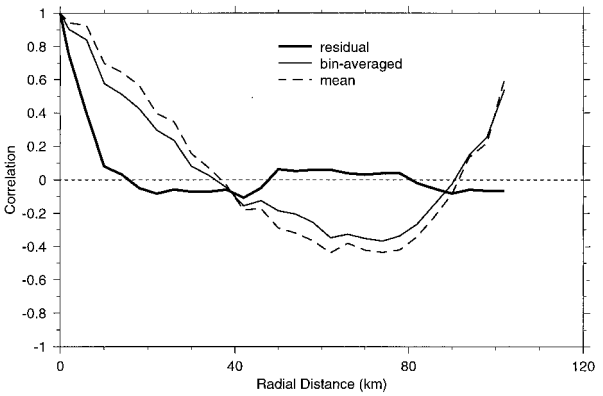

FIG. A1. The depth-averaged spatially lagged autocorrelation for the vertically bin-averaged SeaSoar density data σ_t^{bin} (thin line), the mean density field $\overline{\sigma_t}$ (dashed), and the detided residual density field σ_t^{res} (thick line).

The values of a and b that result from fitting (A1) to the correlation data vary slightly with depth. Table A1 shows the minimum, mean, and maximum values for the correlation parameters. The OA is carried out using the fitted values of a and b at each vertical level. For comparison, recent studies which have applied objective analysis to density (or dynamic height) data from the CCS (e.g., Walstad et al. 1991) obtain a decay scale of 50 km and a zero-crossing of 60 km.

The objective analysis of divergent velocity data to gridded streamfunction requires the specification of an isotropic correlation function for the streamfunction. We

TABLE A1. Residual density field correlation function parameters used in objective analysis.

	a (km)	b (km)
Minimum	20.0	40.0
Mean	22.0	41.2
Maximum	30.0	44.0

use the correlation function for the density field (A1) with the same fitted parameters. The dynamic height correlation function would, in general, be more appropriate for this objective analysis; however, the decay scales and zero-crossings of the density correlation function are not substantially different than the decay scales and zero crossings of the dynamic height correlation function. The longitudinal and transverse velocity correlation functions, derived from (A1), are

$$R(r) = \exp\left(-\frac{r^2}{a^2}\right)\left[\frac{2}{a^2}\cos\left(\frac{\pi r}{b}\right) + \frac{\pi}{br}\sin\left(\frac{\pi r}{b}\right)\right], \quad \text{(A2)}$$

$$S(r) = \exp\left(-\frac{r^2}{a^2}\right)\left\{\left[\frac{2}{a^2}\left(1 - \frac{2r^2}{a^2}\right) + \frac{\pi^2}{b^2}\right] \times \cos\left(\frac{\pi r}{b}\right) - \frac{4r}{a^2}\frac{\pi}{b}\sin\left(\frac{\pi r}{b}\right)\right\}. \quad \text{(A3)}$$

From R and S, we derive the autocorrelation and cross-correlation functions required to perform the objective analysis of ADCP velocity data to form a nondivergent streamfunction:

$$C_{uu} = \cos^2\theta[R(r) - S(r)] + S(r), \quad \text{(A4)}$$

$$C_{vv} = \sin^2\theta[R(r) - S(r)] + S(r), \quad \text{(A5)}$$

$$C_{uv} = \cos\theta\sin\theta[R(r) - S(r)], \quad \text{(A6)}$$

$$C_{u\psi} = \frac{g}{f} r \sin\theta R(r), \quad \text{(A7)}$$

$$C_{v\psi} = \frac{-g}{f} r \cos\theta R(r), \quad \text{(A8)}$$

where g is the gravity constant, f is the Coriolis parameter, and θ is the angle between $\mathbf{r}$ (the separation vector) and the x axis.

REFERENCES

Allen, J. T., and D. A. Smeed, 1996: Potential vorticity and vertical velocity at the Iceland–Færoes Front. *J. Phys. Oceanogr.,* **26,** 2611–2634.

Barth, J. A., 1994: Short-wavelength instabilities on coastal jets and fronts. *J. Geophys. Res.,* **99,** 16 095–16 115.

Bretherton, F. P., R. E. Davis, and C. B. Fandry, 1976: A technique for objective analysis and design of oceanographic experiments applied to MODE-73. *Deep-Sea Res.*, **23,** 559–582.

Brink, K. H., and T. J. Cowles, 1991: The Coastal Transition Zone program. *J. Geophys. Res.,* **96,** 14 637–14 647.

Chelton, D. B., R. A. deSzoeke, and M. G. Schlax, 1998: Geographical variability of the first baroclinic rossby radius of deformation. *J. Phys. Oceanogr.*, **28,** 433–460.

Chereskin, T. K., 1995: Direct evidence for an Ekman balance in the California Current. *J. Geophys. Res.,* **100,** 18 261–18 269.

——, P. T. Strub, C. Paulson, and D. Pillsbury, 1994: Mixed-layer observations at the offshore California Current moored array. *Eos, Trans. Amer. Geophys. Union,* **75**(3), 140.

Chumbinho, R. P. A., 1994: Kinematics and dynamics of a cyclonic eddy off Point Arena, California. Ph.D. dissertation, Naval Postgraduate School, 83 pp.

Cowles, T. J., R. A. Desidiero, and N. Potter, 1994: Steep gradients in phytoplankton biomass in eastern boundary currents: Observations with a multi-excitation spectral fluorometer. *Eos, Trans. Amer. Geophys. Union,* **75**(3), 141.

Denman, K. L., and H. J. Freeland, 1985: Correlation scales, objective mapping, and a statistical test of geostrophy over the continental shelf. *J. Mar. Res.,* **43,** 517–539.

Dewey, R. K., J. N. Moum, C. A. Paulson, D. R. Caldwell, and S. D. Pierce, 1991: Structure and dynamics of a coastal filament. *J. Geophys. Res.,* **96,** 14 885–14 907.

Flament, P., L. Armi, and L. Washburn, 1985: The evolving structure of an upwelling filament. *J. Geophys. Res.,* **90,** 11 765–11 778.

Fofonof, N. P., and R. C. Millard Jr., 1983: Algorithms for computation of fundamental properties of seawater. *UNESCO Tech. Pap. Mar. Sci.*, **44,** 559–582.

Haidvogel, D. B., A. Beckmann, and K. S. Hedström, 1991: Dynamic simulations of filament formation and evolution in the Coastal Transition Zone. *J. Geophys. Res.,* **96,** 15 017–15 040.

Hoskins, B. J., I. Draghici, and H. C. Davies, 1978: A new look at the ω-equation. *Quart. J. Roy. Meteor. Soc.*, **104,** 31–38.

Huntley, M. E., M. Zhou, and W. Nordhausen, 1995: Mesoscale distribution of zooplankton in the California Current in late spring, observed by Optical Plankton Counter. *J. Mar. Res.,* **53,** 647–674.

Huyer, A., and P. M. Kosro, 1987: Mesoscale surveys over the shelf and slope in the upwelling region near Point Arena, California. *J. Geophys. Res.,* **92,** 1655–1681.

——, J. A. Barth, P. M. Kosro, R. K. Shearman, and R. L. Smith, 1997: Upper-ocean water mass characteristics of the California Current, summer 1993. *Deep-Sea Res.,* **45,** 1411–1442.

Kadko, D. C., L. Washburn, and B. Jones, 1991: Evidence of subduction within cold filaments of the Northern California Coastal Transition Zone. *J. Geophys. Res.,* **96,** 14 909–14 926.

Kosro, P. M., 1987: Structure of the coastal current field off northern California during the Coastal Ocean Dynamics Experiment. *J. Geophys. Res.,* **92,** 1637–1654.

——, and A. Huyer, 1986: CTD and velocity surveys of seaward jets off northern California, July 1981 and 1982. *J. Geophys. Res.*, **91,** 7680–7690.

——, A. Huyer, S. R. Ramp, R. L. Smith, F. P. Chavez, T. J. Cowles, M. R. Abbott, P. T. Strub, R. T. Barber, P. Jessen, and L. F. Small, 1991: The structure of the transition zone between coastal waters and the open ocean off northern California, winter and spring 1987. *J. Geophys. Res.,* **96,** 14 707–14 730.

——, A. Huyer, J. A. Barth, R. L. Smith, and P. T. Strub, 1994: Eddies in the California Current region off northern California from satellite and SeaSoar/ADCP measurements. *Eos, Trans. Amer. Geophys. Union,* **75**(3), 141.

——, J. A. Barth, J. Fleischbein, A. Huyer, R. O'Malley, K. Shearman, and R. L. Smith, 1995: SEASOAR and CTD observations during EBC cruises W9306A and W9308B June to September 1993. Data Rep. 160, Ref. 95-2, 393 pp. [Available from College of Oceanic and Atmospheric Sciences, Oregon State University, Corvallis, OR 97331.]

Owens, W. B., 1984: A synoptic and statistical description of the Gulf Stream and subtropical gyre using SOFAR floats. *J. Phys. Oceanogr,* **14,** 104–113.

Paduan, J. D., and P. P. Niiler, 1990: A Lagrangian description of motion in Northern California Coastal Transition filaments. *J. Geophys. Res.,* **95,** 18 095–18 109.

Pedlosky, J., 1987: *Geophysical Fluid Dynamics.* 2d ed. Springer-Verlag, 710 pp.

Pollard, R. T., 1986: Frontal surveys with a towed profiling conductivity/temperature/depth measurement package (SeaSoar). *Nature,* **323,** 433–435.

——, and L. A. Regier, 1992: Vorticity and vertical circulation at an ocean front. *J. Phys. Oceanogr.*, **22,** 609–625.

Rienecker, M. M., and C. N. K. Mooers, 1989: A summary of the OPTOMA program's mesoscale ocean prediction studies in the California Current. *Mesoscale/Synoptic Coherent Structures in*

Geophysical Turbulence, J. C. J. Nihoul and B. M. Jamart, Eds., Elsevier, 519–548.

Rudnick, D. L., 1996: Intensive surveys of the Azores Front. Part II: Inferring the geostrophic and vertical velocity fields. *J. Geophys. Res.*, **101,** 16 291–16 303.

Strub, P. T., P. M. Kosro, A. Huyer, and CTZ Collaborators, 1991: The nature of cold filaments in the California Current system. *J. Geophys. Res.*, **96,** 14 743–14 768.

Walstad, L. J., J. S. Allen, P. M. Kosro, and A. Huyer, 1991: Dynamics of the Coastal Transition Zone through data assimilation studies. *J. Geophys. Res.*, **96,** 14 959–14 977.

Washburn, L., D. C. Kadko, B. H. Jones, T. Hayward, P. M. Kosro, T. P. Stanton, S. Ramp, and T. Cowles, 1991: Water mass subduction and the transport of phytoplankton in a coastal upwelling system. *J. Geophys. Res.*, **96,** 14 927–14 945.

Wyllie, J. G., 1966: Geostrophic flow of the California Current at the surface and at 200 m. *California Cooperative Oceanic Fisheries Investigations Atlas 4.* State of California Marine Research Committee, 288 pp.